Gravitational waves from binary neutron star mergers with a spectral equation of state

Alexander Knight,[1] Francois Foucart,[1] Matthew D. Duez,[2] Mike Boyle,[3]
Lawrence E. Kidder,[3] Harald P. Pfeiffer,[4] and Mark A. Scheel[5]

[1]*Department of Physics and Astronomy, University of New Hampshire,
9 Library Way, Durham, New Hampshire 03824, USA*
[2]*Department of Physics and Astronomy, Washington State University, Pullman, Washington 99164, USA*
[3]*Cornell Center for Astrophysics and Planetary Science, Cornell University, Ithaca, New York 14853, USA*
[4]*Max Planck Institute for Gravitational Physics (Albert Einstein Institute), D-14467 Potsdam, Germany*
[5]*TAPIR, Walter Burke Institute for Theoretical Physics, MC 350-17, California Institute of Technology,
Pasadena, California 91125, USA*

In numerical simulations of binary neutron star systems, the equation of state of the dense neutron star matter is an important factor in determining both the physical realism and the numerical accuracy of the simulations. Some equations of state used in simulations are C^2 or smoother in the pressure/density relationship function, such as a polytropic equation of state, but may not have the flexibility to model stars or remnants of different masses while keeping their radii within known astrophysical constraints. Other equations of state, such as tabular or piecewise polytropic, may be flexible enough to model additional physics and multiple stars' masses and radii within known constraints, but are not as smooth, resulting in additional numerical error. We will study in this paper a recently developed family of equation of state, using a spectral expansion with sufficient free parameters to allow for a larger flexibility than current polytropic equations of state, and with sufficient smoothness to reduce numerical errors compared to tabulated or piecewise polytropic equations of state. We perform simulations at three mass ratios with a common chirp mass, using two distinct spectral equations of state, and at multiple numerical resolutions. We evaluate the gravitational waves produced from these simulations, comparing the phase error between resolutions and equations of state, as well as with respect to analytical models. From our simulations, we estimate that the phase difference at the merger for binaries with a dimensionless weighted tidal deformability difference greater than $\Delta\tilde{\Lambda} \approx 55$ can be captured by the spectral Einstein code for these equations of state.

I. INTRODUCTION

Great progress has been made in gravitational wave astrophysics starting with the binary black hole (BBH) merger event GW150914 [1] and the detection of the binary neutron star merger event GW170817 by the LIGO/Virgo/KAGRA collaboration [2]. Additional mergers of black hole-neutron star (BHNS) and binary neutron star (BNS) have been observed, such as GW190425 [3], GW200115 [4], and GW191219 [5]. We have also observed merger events between objects with properties outside of what was previously expected, such as GW190814 [6], which has either the heaviest neutron star (NS) or lightest black hole (BH) detected so far, with a mass of $2.50 - 2.67 M_\odot$, partnered with a $22.2 - 24.3 M_\odot$ BH. Gravitational waves from these mergers carry information about the system's chirp mass, as well as the angular momentum and mass of each compact object. In the presence of a neutron star, they also provide information on how matter behaves at densities higher than nuclear saturation density.

To interpret this information, we need to quickly generate millions of theoretical gravitational wave signals. Even with modern methods and technologies, however, creating simulations that sample the available parameter space densely enough to allow us to perform parameter estimation on observed binaries remains prohibitive in time and computational cost. As a result, simulations are instead used to test and/or train analytical models. While analytical models have high accuracy during the inspiral of a binary even without including any information from merger simulations, they can become inaccurate in the last few orbits before the merger—which also happens to be when the impact of the finite size of a neutron star is most noticeable on the waveform. Numerical relativity simulations are thus used to test or calibrate these models for better accuracy during these critical stages of a merger event. As the accuracy of these analytical models (or, at the very least, our ability to test said accuracy) is then dependent on the accuracy of merger simulations,

023034-1

a reduction of potential numerical errors below the expected accuracy of current and future gravitational wave detectors is highly desirable. For GW170817, the only event so far to put meaningful constraints on the equation of state (EOS) of dense matter, modeling errors were most likely unimportant [2]. However, with planned improvements to the sensitivity of current detectors and the construction of new observatories, the frequency of gravitational wave detections will increase, and modeling errors will potentially become an important source of uncertainty.

In the case of BNS mergers, high-accuracy simulations are still relatively new, and even the best simulations have a lower accuracy and a higher computational cost than for BBH mergers. BNS mergers require the evolution of the equations of general relativistic hydrodynamics in addition to Einstein's equations. Beyond the cost of evolving this additional system of equations, the presence of surface discontinuities and/or shocks in the fluid makes it impossible to use for neutron star mergers the high-order methods that have allowed BBH simulations to produce high-accuracy waveforms at a reasonable computational cost, or at least impossible to consistently use such methods across the entire computational domain.

There are at least two ways to limit the unphysical impacts of discontinuities in the evolution of the fluid. One is the use of numerical methods capable of maintaining high-order accuracy while capturing shocks and surfaces. Methods demonstrating third-order convergence (for composition-independent EOSs) [7] and fourth-order convergence (for piecewise polytropes) [8] in the phase of the gravitational wave signal have been published so far.[1] The other is to improve the smoothness of the EOS used to describe high-density matter [9,10]. Smoother EOSs typically lead to lower truncation errors. A simple $\Gamma = 2$ polytropic EOS, for example, is much preferable in terms of numerical accuracy to the more complex piecewise-polytropic EOS, or to the tabulated, composition and temperature-dependent EOS needed in simulations that evolve neutrinos or that aim to capture changes in the fluid composition. There is however a significant trade-off, in that a simple polytropic EOS matching the desired mass and radius of a specific neutron star will often not be consistent with known physical constraints, for example, the maximum mass of neutron stars, or the radius of neutron stars of different masses. Additionally, these simple EOSs are much farther from satisfying constraints on the nuclear EOS derived from theoretical and experimental nuclear physics results. With constraints on the neutron star from studies such as [11–15], a smooth EOS that is more consistent with at least the known physical constraints on

the macroscopic properties of cold neutron stars (mass-radius relation, maximum mass) is desirable. Several other methods have been developed to approach these issues. O' Boyle *et al.* (2020) [16] has modified a piecewise-polytropic EOS to be smoothly differentiable. Legred *et al.* (2023) [17] uses a flexible parameterized-enthalpy EOS, demonstrating the ability to balance numerical cost with accurate behavior. The latter EOSs are effectively an extension of the EOS used here, aimed in large part at improving the ability of smooth equations of state to capture more rapid changes in the pressure-density relation. Similarly, one advantage of smoothed piecewise-polytropes over spectral equations of state would be the ability to use relatively short smoothing lengths to capture rapid changes in the pressure. When used in numerical simulations, sharper features, even if mathematically smooth, are however likely to lead to a loss of accuracy if the smoothing length is short compared to the numerical resolution. In this manuscript, we limit ourselves to evaluate our ability to perform high-accuracy simulations with the simple spectral equations of state of [9]. Using these alternative models would likely lead to similar accuracy for the subset of these equations of state devoid of underresolved features.

We note that while this spectral equation of state allows us to construct an EOS that more closely matches any chosen set of constraints on the properties of cold matter in beta equilibrium, the temperature dependence of our EOS remains extremely simplified, and it does not include any composition dependence [9]. A method to expand a cold, beta-equilibrium EOS with a more physically motivated temperature and composition dependence has been proposed in [18,19], but is not currently implemented in the spectral Einstein code (SpEC) used in this work. Our ability to accurately evolve these spectral EOSs was first tested in [9] over short simulations; this manuscript presents our first full inspiral-merger simulations using these EOSs. As we are in particular interested in estimating our ability to capture tidal effects in waveforms, this manuscript includes simulations of systems with identical neutron star masses but performed with two EOSs with ∼20% differences in their dimensionless tidal deformability (∼570 vs ∼710 for GW170817-like systems). We will show that the phase difference between the resulting waveforms at the merger is resolved in our simulations.

In addition to our study of this spectral EOS, we will in this manuscript evaluate the performance of a new time stepping method for SpEC evolutions, where the evolution of Einstein's equations is permitted to take smaller steps than the evolution of the fluid equations. For the SpEC code, this offers reduced computational cost, as these two systems of equations are evolved on different numerical grids, with different time step constraints. The fluid equations are typically more costly to solve in each individual time step, while Einstein's equations often require a shorter step to reach a desired accuracy.

---

[1]We note that piecewise polytropic equations of state are composition-independent EOSs, but the reverse is not necessarily true. The methods used in [7] are applicable in any simulation in which the composition of the fluid is not evolved, while those of [8] make more restrictive assumptions for the form of the EOS.

Here, we demonstrate that uncoupling these time stepping systems results in simulations equivalent (within expected numerical errors) to those obtained when Einstein's equations, and the equations of hydrodynamics use the same time stepping algorithm. We note that this is largely due to the fact that time stepping errors are subdominant in SpEC. The time step size is determined by stability considerations rather than to reach a specific accuracy target, and time stepping errors are significantly smaller than spatial discretization errors in our simulations, for all time stepping algorithms considered here.

We simulate six distinct physical configurations, using two different EOSs each evolved at three mass ratios. For two of these cases, we also use both time stepping methods. We then extrapolate the gravitational waves to future null infinity and compare these gravitational waves to analytical models. All waveforms presented here will become public as part of the next data release by the SxS collaboration.

II. METHODS

A. Evolution

For the simulations presented in this manuscript, we use the Spectral Einstein Code (SpEC) [20], which evolves Einstein's equations using the generalized harmonic formalism [21] on a pseudospectral grid, with p-type adaptive mesh refinement [22]. The general relativistic hydrodynamical equations are evolved on a separate grid using the high-order shock capturing scheme described in Radice and Rezzolla (2012) [23]. This scheme uses the fifth-order, shock capturing MP5 reconstruction to interpolate from cell centers to cell faces, and a Roe solver to calculate numerical fluxes at cell faces. It has been shown to result in third-order convergence of the solution when used in neutron star merger simulations [23].

Einstein's equations and the fluid equations are both evolved in time using a third-order Runge-Kutta algorithm. In the algorithm previously used in SpEC, both systems of equations use the same time step, chosen to meet a target time discretization error (see Appendix A, Sec. 3 of [24]). Practically, this usually results in a time step that is just small enough to match the stability condition of our time stepping algorithm, as below that stability limit, the time stepping error is much smaller than our target accuracy. Coupling source terms are communicated between the grids at the end of each time step. Linear extrapolation from the current step and previous steps is used to determine the values of the source terms during the intermediate steps of the Runge-Kutta algorithm.

In previous SpEC simulations, the time steps on the two grids were always identical, $\Delta t_f = \Delta t_{GR}$, where Δt_f is the time step increment of the fluid grid, and Δt_{GR} is the time step increment of the grid evolving Einstein's equations. In the new algorithm used in some of the simulations presented here, the fluid equations take a time step

$\Delta t_f = \alpha_{\mathrm{CFL}} \min(\frac{\Delta x_{\mathrm{FD}}}{c_{\max}})$, with Δx_{FD} the grid spacing on the fluid grid, $c_{\max}$ the maximum characteristic speed of the fluid equations in grid coordinates in a cell (in absolute value), and $\alpha_{\mathrm{CFL}} = 0.25$ a constant chosen to maintain stability of the evolution. The minimum is taken over all cells in our computational domain. The time step used for Einstein's equations is again chosen to meet the time discretization error, which practically sets Δt_{GR} at a value appropriate for stability of the evolution on the pseudospectral grid. In general, $\Delta t_f > \Delta t_{GR}$, and Δt_{GR} is similar to the time step used when both grids were required to take identical time steps. In the new time stepping method, we now allow the code to take multiple steps on the pseudospectral grid for each step on the fluid grid. We require the end of a time step on the fluid grid to match the end of a time step of the metric evolution. The code thus takes advantage of the fact that the stability condition on the time step size is less restrictive on the finite difference grid than on the pseudospectral grid.

In this new method, source terms are communicated between the two grids at the end of each time step of the fluid evolution. This results in less frequent communication than in our previous algorithm and in a lower number of time steps for the fluid equations. At intermediate times, we again use extrapolation from previous time steps to calculate the source terms. The order of extrapolation used in this algorithm is freely specifiable. So far, we found no significant impact on the accuracy of our simulations as long as we use at least first-order extrapolation. In the rest of this manuscript, we will refer to the simulations using the same time step on both grids as *shared time step* (ShTS), and the simulations using a different time step on each grid as *split time step* (SpTS).

In order to test the impact of the time stepping algorithm on accuracy, we evolved a BNS system for 0.35 ms starting from the same simulation snapshot, but using either the ShTS and SpTS algorithm. For each algorithm, we evolved with our time step for medium resolution simulations, as well as with time steps 2 and 4 times smaller. In all cases, the observed time discretization errors were orders of magnitude smaller than spatial discretization errors over comparable time scales (relative errors in the phase of the orbital trajectory $\lesssim 10^{-8}$ in all cases and showing first-order convergence, likely due to errors on the surface of the neutron star or in the atmosphere that become dominant for such small errors). In SpEC simulations of BHNS and BNS systems, the time step is limited by stability considerations, not by accuracy considerations. As a result, a time-stepping algorithm such as ShTS, which slightly increases time-stepping errors while reducing simulation cost, is desirable, as the practical impact of the chosen algorithm on the overall error budget remains negligible.

Interpolating from the spectral grid to the finite-difference grid to communicate source terms is done by refining the spectral grid by approximately a factor of 3 in

each dimension and then using third-order polynomial interpolation from the colocation points in the refined spectral grid to the finite-difference grid. Interpolation from the finite-difference grid to the spectral grid uses fifth-order polynomial interpolation, limited so that interpolation does not create any new extremum in the fluid variables.

The pseudospectral and finite difference grids both rotate and contract to follow the binary system. The finite-difference grid is rescaled when the grid spacing decreases by a factor of 0.8 in the inertial frame, in order to keep a consistent resolution during all phases of the evolution. The finite-difference grid removes subdomains where no significant matter [$\max(\rho) < 6.2 \times 10^9 \, \frac{\text{g}}{\text{cm}^3}$] is located and adds back subdomains as higher density matter flows close to the boundary of the removed subdomains over the course of the simulation. These two methods result in a reduced computational cost for our simulations.

For a full explanation on SpEC's methods for the evolution of the hydrodynamical and general relativistic grids, we refer the reader to Duez *et al.* (2008) [25], as well as Appendix A of Foucart *et al.* (2013) [24]. We will limit ourselves here to a brief discussion of the methods most relevant to the use of spectral EOSs in simulations aiming to produce high-accuracy numerical waveforms.

We define the neutron star matter as a perfect fluid with stress-energy tensor

$$T^{\mu\nu} = (\rho + u + P)u^\mu u^\nu + Pg^{\nu\mu}. \tag{1}$$

In this equation, we have the pressure P, baryon density ρ, internal energy density u, four-velocity u^μ, and the inverse metric $g^{\mu\nu}$. The evolution equations are derived from the conservation of baryon number[2]

$$\nabla_\mu(\rho u^\mu) = 0, \tag{2}$$

and the energy-momentum conservation

$$\nabla_\mu T^{\mu\nu} = 0, \tag{3}$$

which give give equations for six independent variables (e.g., ρ, u, P, and three independent components of the velocity). We close the system of equations with an EOS, which introduces two functions $P(\rho, T)$ and $u(\rho, T)$ (defined below), with temperature T. While such an EOS introduces T as a new variable, the two equations, $P(\rho, T)$ and $u(\rho, T)$, are sufficient to close the system of equations.

---

[2]The baryon density is defined as $\rho = m_b n$, with n the baryon number density and m_b an arbitrarily chosen reference mass for baryons; accordingly, our evolution equation represents conservation of baryon number, not conservation of mass.

Practically, we evolve the "conserved" variables

$$\rho_* = -\sqrt{\gamma} n_\mu u^\mu \rho, \tag{4}$$

$$\tau = \sqrt{\gamma} n_\mu n_\nu T^{\mu\nu} - \rho_*, \tag{5}$$

$$S_k = -\sqrt{\gamma} n_\mu T^\mu_k, \tag{6}$$

where γ is the determinant of the spacial metric $\gamma_{ij} = g_{ij} + n_i n_j$, and n^μ is the future directed unit normal to a constant time slice. The integral of ρ_* ("total baryonic mass") is conserved over the entire domain, up to losses at the domain boundary. Recovering the "primitive" variables (ρ_0, T, u_i) from the conserved variables requires multidimensional root finding. We follow the 2D root-finding method of Noble *et al.* [26], with corrections in low-density and high-velocity regions where due to numerical errors in the conservative variables, the inversion may not be possible [24]. The evolution equations are written in "conservative" form, i.e., as a set of five coupled equations of the form

$$\frac{\partial \mathbf{F}^0(\mathbf{u})}{\partial t} + \sum_{i=1}^{3} \frac{\partial \mathbf{F}^i(\mathbf{u})}{\partial x^i} = \mathbf{S}(\mathbf{u}), \tag{7}$$

with the primitive variables $\mathbf{u}$, vector of conserved variables $\mathbf{F}^0(\mathbf{u})$, fluxes $\mathbf{F}^i$, and source terms $\mathbf{S}(\mathbf{u})$. These fluxes and source terms are calculated at cell centers, and the fluxes (as well as the physical variables ρ_0, T, and u_i) are interpolated to cell faces. The calculation of the divergence of the fluxes from the values of $\mathbf{u}$ at cell centers follows the previously mentioned method of Radice and Rezzolla [23].

B. Numerical implementation of the spectral equation of state

The EOS used in these simulations to describe matter inside the neutron star was developed in Lindblom (2010) [27], and modified in Foucart *et al.* (2019) [9] for computational use. As already mentioned, the choice of EOSs in numerical simulations is often a trade-off between the ability to capture more physics and a wider range of possible models on one side, and the numerical accuracy of the simulations on the other side. Spectral EOSs are smoother than both tabulated and piecewise polytropic EOSs, which results in higher accuracy simulations (as will be seen in the results section). On the other hand, our existing spectral EOSs are limited to matter in beta equilibrium, use an extremely simplified model for the thermal pressure, and are not suitable for coupling to neutrino evolution. We consider this a reasonable trade-off when attempting to generate high-accuracy gravitational wave signals from the inspiral, merger, and early postmerger evolution of BNS and BHNS binaries, but acknowledge that spectral EOSs would be a poor choice

for simulations attempting, e.g., to model the outcome of *r*-process nucleosynthesis in mergers. Single polytropic EOSs, for their part, lead to higher accuracy simulations than more complex spectral EOSs at a given resolution.[3] However, their use to simulate asymmetric binaries and/or the merger and postmerger phase of the evolution of a binary may be problematic. Indeed, while it is possible to construct a single polytropic EOS for which a neutron star of a given mass has the desired radius, or the desired tidal deformability, it is typically difficult to do this for two neutron stars of distinct mass or to make sure that the EOSs at the same time support massive neutron stars $M_{NS} \gtrsim 2M_{\odot}$.

In this section, we give a reduced explanation of the theory of spectral EOS. A full explanation can be found in the previous work by Foucart *et al.* (2019) [9] and Lindblom (2010) [27].

We choose the spectral expansion as in Foucart *et al.* (2019) [9] by writing the pressure P and specific internal energy ϵ as

$$P(x,T) = \begin{cases} P_0 \exp\left(\Gamma_0 x + \eta_2 \frac{x^3}{3} + \eta_3 \frac{x^4}{4}\right) + \rho T & x > 0 \\ P_0 \exp(\Gamma_0 x) + \rho T & x \leq 0 \end{cases}, \quad (8)$$

and

$$\epsilon(x,T) = \begin{cases} \epsilon_0 + \int_0^x d\xi \frac{P(\xi,0)}{\rho_0} e^{-\xi} + \frac{T}{\Gamma_{th}-1} & x > 0 \\ \frac{P(x,0)}{\rho(\Gamma_0-1)} + \frac{T}{\Gamma_{th}-1} & x \leq 0 \end{cases}, \quad (9)$$

with some reference density ρ_0, reference adiabatic index Γ_0, reference pressure P_0, temperature T, and where we define $x = \log\left(\frac{\rho}{\rho_0}\right)$. We note that despite its name, used here to match standard conventions, T does not scale linearly with the physical temperature of the fluid; it is simply defined so that the thermal pressure is $P_{thermal} = \rho T$.

These equations give free parameters of η_2, η_3, ρ_0, P_0, and Γ_0. Many possible sets of values for these would result in sound waves in dense matter moving at superluminal velocities and/or behavior that does not conform to known nuclear physics. In Foucart *et al.* (2019) [9], a Marko-Chain Monte Carlo method was used to determine values of these parameters resulting in causal EOSs, and values of the pressure at high-density within the range of values currently allowed by nuclear physics. We also found that the choice $\Gamma_0 = 2$ led to higher accuracy than lower values of Γ_0, possibly due to the simple behavior of the density close to the surface for that choice of Γ_0. We make this choice here as well, even though this results in values of the

pressure and internal energy at $\rho \ll \rho_0$ that are inconsistent with the known behavior of dense neutron rich matter at low density. This is reasonable for our purpose here because the gravitational wave signal is mostly sensitive to the EOS at high density. From [9], we choose two EOSs with free parameters shown in Table I, with mass-radius curves shown in Fig. 1. The first EOS parameter set displays a higher maximum mass and lower maximum radius (hMlR), while the second has a lower maximum mass and a higher maximum radius (lMhR). The hMlR EOS gives neutron stars with a maximum Schwartzschild radius of 12.05 km and maximum baryonic mass of $2.719M_{\odot}$, while the lMhR EOS gives neutron stars with a maximum Schwartzschild radius of 12.41 km and maximum baryonic mass of $2.191M_{\odot}$.

C. Initial conditions

For both the ShTS and SpTS time stepping algorithm, we evolve binary neutron star systems with the same chirp mass $M_{chirp} = 1.18M_{\odot}$, chosen to match the chirp mass of GW170817. Our chosen configurations for the ShTS method consist of two systems, with mass ratios of $q = 1.1$ and $q = 1.2$ and the hMlR EOS, separated by a distance of 53.1 km, and no initial neutron star spin. The SpTS simulations have mass ratios of $q = 1.0$, $q = 1.1$, and $q = 1.2$, separated by 54.6 km, with no initial spin, and are performed for both EOSs. We construct out initial data utilizing our SPELLS code [28] adapted for binary neutron star systems [29,30], which generates a binary system in quasicircular orbit. From this, we iteratively adjust the initial angular and radial velocity of the neutron stars to reduce the initial eccentricity of the orbits to $\lesssim 0.002$ utilizing the methods of Pfeiffer (2007) [31]. With these methods, and initial separation distance, we reach the merger at about 10.5 orbits for the ShTS and about 11.5 orbits for the SpTS. Parameters for all simulations can be found in Table II.

With these EOSs, we have two systems with a mass averaged dimensionless tidal deformability $\tilde{\Lambda} \approx 570$ for the hMlR EOS and $\tilde{\Lambda} \approx 710$ for the lMhR EOS. For the hMlR EOS, the dimensionless tidal deformabilities ranges are $\Lambda_1 = 319–588$ and $\Lambda_2 = 588–991$, and the lMhR EOS ranges from $\Lambda_1 = 530–714$ and $\Lambda_2 = 714–1224$. These values rest comfortably within the 90% probability region of low spin systems (and very close to the 50% region in some cases) for the Λ_1 and Λ_2 relationship from the LIGO and Virgo constraints [32]. We choose values of Λ at the high end of those regions to maximize tidal effects.

D. Domain/grid setup

The initial finite-difference hydrodynamical domain construction consists of a rectangular, bar-shaped Cartesian grid space with the neutron stars located at each end. We have three resolutions for the $q = 1.1$ and $q = 1.2$ hMlR

---

[3]Or at least than the spectral EOS used in this manuscript; single polytropic EOSs are themselves a subset of the spectral models but one that does not allow much flexibility on the functional form of the EOS.

TABLE I.   Spectral EOS parameters used in this manuscript. Mass-radius curves for these EOS parameter sets can be seen in Fig. 1.

EOS	Γ_0	η_2	η_3	Γ_{th}	$\rho_0 \frac{g}{cm^3}$	$P_0 \frac{dyn}{cm^2}$
hMlR	2.0	0.45872	-0.114849	1.75	5.07405×10^{13}	$1.637887436 \times 10^{35}$
lMhR	2.0	0.435096	-0.111447	1.75	3.33533×10^{13}	5.8481×10^{34}

ShTS and the $q = 1.0$ lMhR SpTS simulations (i.e., the first, second, and sixth simulations of Table II). For the $q = 1.1$ and $q = 1.2$ simulations, we have grid spacings for the finite difference domain of $\Delta x_{FD} = 298$ m, 239 m, 191 m with number of grid points along the length of each axis of $(369 \times 185 \times 185)$, $(457 \times 229 \times 229)$, and $(577 \times 289 \times 289)$, respectively. The $q = 1.0$ simulation has grid spacings of $\Delta x_{FD} = 273$ m, 218 m, and 174 m, with grid points of $(401 \times 201 \times 201)$, $(505 \times 253 \times 253)$, and $(649 \times 325 \times 325)$, respectively. For future ease, we will refer to the lowest resolution of each simulation set as
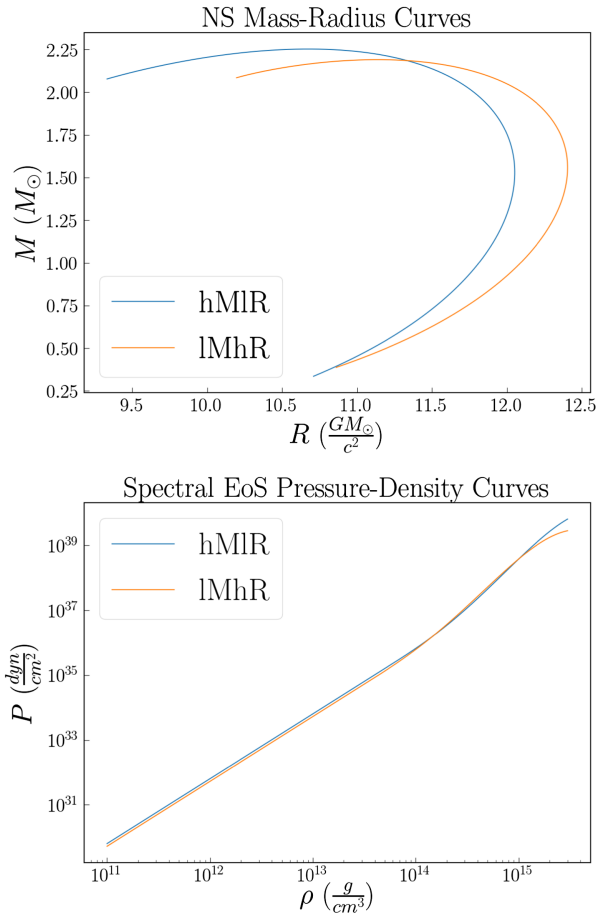

FIG. 1.   Mass-radius and pressure-density curves for our EOS parameter sets. We label these EOSs by their behavior on these plots, with the blue curve having a higher maximum mass, but lower maximum radius, and as such abbreviated as hMlR. We label the orange curve to lMhR in a similar fashion. Both EOSs behave similarly at densities lower than $\sim 10^{14}$ g cm^{-3} but significantly differ above 10^{15} g cm^{-3}.

LR, the middle MR, and the highest resolution HR. The SpTS hMlR EOS simulations (third, fourth, and fifth simulations of Table II) were run at the MR resolution, while the SpTS lMhR $q = 1.1$ and $q = 1.2$ (last two simulations of Table II) were run at the MR and HR resolutions.

In the SpTS simulations, we no longer use the same grid spacing for all simulations. Instead the grid spacing is chosen so that we have $N = (72, 90, 112)$ grid points across the diameter of the neutron stars at LR, MR, and HR respectively, averaging over both stars at $t = 0$.[4] The domain then is the smallest box covering spheres of radius $0.75(R_1 + R_2)$ around each neutron star, with R_1, R_2 the coordinate radii of the neutron stars. This domain is divided into eight equal segments along the shorter axis and 16 segments along the long axis, resulting in 512 subdomains of equal size. This method has the advantage of automatically adapting the initial numerical resolution to the size of the neutron star in the initial data. For the neutron stars evolved in this manuscript, this results in higher numerical resolution than in the equivalent ShTS simulations: Effectively, the LR SpTS grids are halfway between the LR and MR grids of the ShTS simulations. The lower cost of the SpTS algorithms allows us to do this while still reducing the cost of the simulations (see end of Sec. III).

The spectral grid construction consists of a ball and five shells covering each of the neutron stars. A set of distorted cylinders, with the rotational axis along the line between the neutron stars, connects the sets of ball and shells around the neutron stars. These cylinders also connect to 12 shells covering the outer regions, which are centered on the center of mass of the system. After the merger, the area interior to the outer shells (the area previously covered by the balls, accompanying shell sets, and distorted cylinders) is replaced by distorted cubic subdomains. We refer the reader to Foucart *et al.* (2013) [24] and Szilágyi (2014) [22] for a more detailed explanation and graphics of the pseudospectral grid construction. The number of basis functions used in each subdomain is adaptively chosen to reach a user-defined maximum error, which is estimated from the spectral coefficients of the evolved variables.

---

[4]The grid spacing quoted above for the SpTS lMhR simulation are the result of this choice. Note that our initial data is in a coordinate system close to isotropic coordinates, in which the neutron star radius is smaller than in Schwarzschild coordinates. Hence, $N \times \Delta x \neq 2R_{NS}$ if R_{NS} is the areal (Schwarzschild) radius used, by convention, in our description of the neutron stars.

TABLE II.   From left to right, we have the time stepping method, mass ratio q, the EOS (see Table I), ADM mass in units of solar masses M_1 and M_2, areal radii in km R_1 and R_2, initial separation in km d, initial angular velocity Ω_0 in Hz, dimensionless tidal deformability Λ_1 and Λ_2, and the weighted average tidal deformability $\tilde{\Lambda}$.

Time step	q	EOS	M_1 ($M_\odot$)	M_2 ($M_\odot$)	R_1 (km)	R_2 (km)	d (km)	Ω_0 (Hz)	Λ_1	Λ_2	$\tilde{\Lambda}$
ShTS	1.1	hMlR	1.4267	1.2970	12.0	12.0	53.1	225	424	766	573
ShTS	1.2	hMlR	1.4910	1.24254	12.1	12.0	53.1	225	319	989	572
SpTS	1.0	hMlR	1.3600	1.3600	12.0	12.0	54.6	216	588	588	588
SpTS	1.1	hMlR	1.4268	1.2971	12.0	12.0	54.6	216	424	767	573
SpTS	1.2	hMlR	1.4911	1.2426	12.1	12.0	54.6	216	319	991	573
SpTS	1.0	lMhR	1.3600	1.3600	12.4	12.4	54.6	216	714	714	714
SpTS	1.1	lMhR	1.4268	1.2971	12.4	12.3	54.6	216	530	950	713
SpTS	1.2	lMhR	1.4911	1.2426	12.4	12.3	54.6	216	399	1220	711

The user-defined accuracy on the pseudospectral grid is chosen such that it scales as $(\Delta x_{\mathrm{FD}})^5$, and as such errors on this grid converge faster than those on the finite-difference hydrodynamical grid.

E. Waveform extrapolation

The simulations evolve through the inspiral, plunge, and merger and then continue until the peak of the gravitational waves resulting from the merger event progress past the outer edge of the pseudospectral grid at a radius of 2047.5 km for the ShTS simulations and 2074.7 km for the SpTS simulations.

The method to extrapolate the gravitational wave signal to null infinity from the metric at finite radii follows the procedure outlined by Boyle and Mroue (2009) [33]. The Newman-Penrose scalar Ψ_4 and metric perturbation h are estimated on spheres of constant inertial radii and decomposed into spin $= -2$ spherical harmonics components. At 24 radii from $R_i = 211.2$ km to $R = 2,015.6$ km equidistant in $1/R$, we compute a retarded time $t_{\mathrm{ret}}(t, R_i)$ to approximate the travel time for the wave from the merging neutron stars to R_i. From here, we fit the ansatz

$$A_{lm}(t_{\mathrm{ret}}, r) = \sum_{j=0}^{N} A_{lm,j}(t_{\mathrm{ret}}) r^{-j}, \qquad (10)$$

$$\phi_{lm}(t_{\mathrm{ret}}, r) = \sum_{j=0}^{N} \phi_{lm,j}(t_{\mathrm{ret}}) r^{-j}, \qquad (11)$$

to the amplitude A_{lm} and phase ϕ_{lm} of the (l, m) component of the spherical harmonic decomposition of the gravitational wave at fixed retarded times. We then estimate the (l, m) mode at infinite radius to be $A_{lm,1} e^{i\phi_{lm,0}}$.

III. RESULTS

A. Error analysis

We begin the discussion of our results with an overview of the methods used to verify the quality of the simulations

and a discussion of our methods to estimate errors. First, we can consider diagnosis of the numerical dissipation in the evolution of the fluid. The thermal energy is a good proxy for the amount of dissipation during inspiral—while there should be a small amount of physical heating due to tides in the neutron stars, in current simulations, heating from numerical dissipation is dominant. We can see the evolution of the specific internal energy (as a fraction of the rest mass energy) at three resolutions on Fig. 2. It shows clear convergence toward zero before the merger, with an order of convergence between second and third order. During and after the merger, the heating is physical and thus does not converge to zero. Other diagnosis of the evolution of the fluid, not shown here but behaving as expected, include the
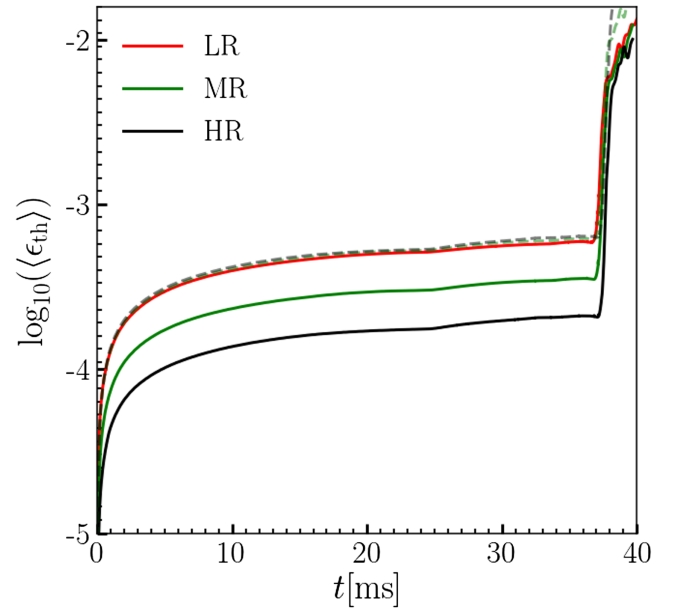

FIG. 2.   Mass weighted average of the specific thermal energy for the equal mass, SpTS simulation of the lMhR equation of state [i.e., $\epsilon_{\mathrm{th}} = \epsilon(\rho, T) - \epsilon(\rho, 0)$]. The dashed curves are rescaled assuming convergence to zero with order $n = 2.5$. Before the merger, we see clear convergence of the numerical heating with increased resolution.
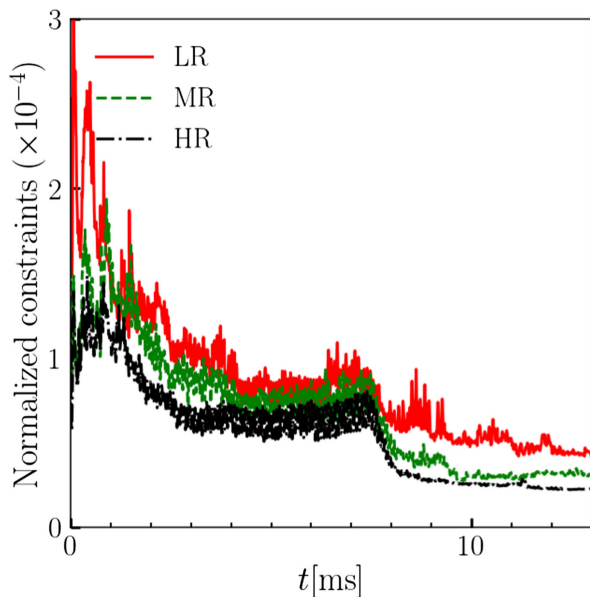
FIG. 3. Normalized constraints for the first ~13 ms of evolution, for the $q = 1.1$ configuration, lMhR equation of state, and SpTS time stepping. Simulations were run until the constraints leveled out, as original simulations performed at three resolutions did not archive constraint violation information. The first ~7 ms of evolution is dominated by the constraint violation from the initial conditions propagating out.

evolution of the central density of the star (which oscillates at a fixed frequency due to the initial data being slightly out of hydrostatic equilibrium and additionally decreases over time due to dissipation) and the conservation of baryon number.

For the evolution of the metric, we can look at constraint violations in the evolution of Einstein's equations. On Fig. 3, we plot the *normalized constraint* defined in Eq. (71) of [21], which effectively measures the level of constraint violations across all constraints in the generalized harmonic formalism. Initially, small errors in the initial conditions dominate the constraint violations, propagating outward. After ~7 ms, most of the constraint violating modes reach the outer boundary of the domain and leave the grid. At later times, the constraints are set in part by numerical errors in the evolution of Einstein's equations and in part by reflection of the constraints at the outer boundary. They then settle to a near constant value. Due to the presence of constraint violations in the initial data, we do not expect clean high-order convergence of the constraints to zero, but we do expect lower constraints at higher resolution, as observed.

We can now move to estimates of the error on the gravitational wave signal. We rely on a conservative error estimate presented in Foucart *et al.* (2019) [9] and Foucart *et al.* (2021) [34] that likely overestimates the potential errors in order to account for the difficulty of exactly measuring errors in dual-grid SpEC simulations. We take

into account three potential sources of error in our simulations: finite resolution of our computational domain, extrapolation of the gravitational wave to infinity, and mass lost during the simulation at the boundaries—although the former turns out to nearly always be the dominant source of error. For a more detailed overview of how these error sources are evaluated, we recommend Foucart (2019) [9], but we will review the fundamentals here and show the error estimates for the (2,2) mode of the extrapolated waveforms.

We estimate the errors due to finite resolution by comparing the three resolutions, LR, MR, and HR. First, we use the phases of the LR and HR simulations in a Richardson extrapolation to infinite resolution, assuming a second-order convergence. We then take the difference between the HR waveform and the extrapolated waveform as a first estimate of the numerical error. We repeat this process on the HR and MR resolutions and keep the worst of these two error estimates. We note that this is typically conservative because the methods used within the SpEC code individually converge at better than second order. However, the hybrid spectral/finite volume methods utilized by SpEC causes different errors to dominate at different phases of the simulation. In particular, finite difference errors typically drive the system to inspiral faster, while errors on the pseudospectral grid can lead to slower inspiral [25] or impact the initial eccentricity (which may cause the system to inspiral faster or slower). As a result, when considering only two resolutions, it is not uncommon for multiple sources of error to cancel each other, especially as the simulation setup is chosen so that neither the spectral error nor the finite difference error dominates at all times and all resolution. This leads to a more efficient use of computational resources, but also to more complex behavior of the error as we increase resolution, as during a simulation. Practically, we do not have a single dominant source of error with a consistent sign. This is in contrast to purely finite difference simulations, where phase errors are dominated by numerical dissipation that accelerates the inspiral, and which accordingly usually converge monotonously to the correct answer, allowing for cleaner error measurements. This is a clear disadvantage of the hybrid methods used in SpEC. The advantage of the hybrid spectral-finite difference method, on the other hand, is that we benefit from the efficiency and high accuracy of spectral methods in regions where the solutions is smooth and only need to evolve with finite difference methods the small regions covering the two neutron stars.

Given the less robust nature of error estimates for the hybrid method, we only consider those estimates reliable if they are confirmed by multiple diagnosis. Part of this process is the dependence of thermal heating and constraint violations on resolution (see above), which more directly tests the fluid and metric evolution. More importantly

however is the fact that similar errors are consistently predicted for multiple simulations using a range of initial configurations but similar numerical methods and that simulations performed with different numerical methods provide results consistent within our predicted numerical errors (as estimated using the method described earlier in this section). Tests along both of those axes are performed in this manuscript. We will see additionally that waveforms matched at the time of the merger show second-order convergence for the phase of the waveform, most likely because numerical dissipation is the dominant source of error at late times (see, e.g., Fig. 10). This is a particularly important diagnostic considering that waveforms matched at late times are also what we rely on to compare simulations and models.

The errors from extrapolation to null infinity are estimated by comparing the phase difference between the second- and third-order extrapolation in r^{-1}, between $t = 0$ and t_{peak}, where the (2, 2) mode of the waveform reaches its maximum amplitude. The maximum phase difference is conservatively chosen to be the associated error. This error is typically smaller than the finite resolution error, except at the very beginning of a simulation.

Finally, mass lost during the evolution results in gravitational waves emitted from a system different from the initially intended system. Here, we use an estimate of the resulting error in the phase of the waveform derived in Boyle (2007) [35]. In our simulations, mass loss was minimal and resulted in a negligible phase error comparative to the error from finite resolution. The $q = 1.1$ ShTS simulation lost approximately $5.42 \times 10^{-6} M_\odot$ while the $q = 1.2$ simulation lost approximately $8.71 \times 10^{-6} M_\odot$. The lMhR $q = 1.0$ SpTS simulation lost $1.52 \times 10^{-5} M_\odot$. The other SpTS simulations were performed at either one or two resolutions, as opposed to the three required for the previous error analysis. The simulations with two resolutions demonstrated similar phase difference between resolutions as the $q = 1.0$ lMhR SpTS.

In Fig. 4, we can see the three sources of error, as well as the total error ϕ_T. In all of these figures, clearly the finite resolution error (ϕ_{dis}) of the simulation dominates ϕ_T from

a few hundred t/M after the start of the simulation to past the merger. At the time of the merger, the hMlR ShTS $q = 1.1$ and $q = 1.2$ simulations have approximately one to two radians of phase error, but the longer lMhR SpTS $q = 1.0$ simulation peaks at approximately four radians at the time of the merger. Overall, we find consistent error estimates for all configurations, with the length of the simulation being the main determinant of the total error, as expected when using similar numerical methods and equations of state. The extrapolation error (ϕ_{ext}) provides a constant error estimate at approximately 0.01 radians, 2 orders of magnitude smaller than the discretization error at the time of the merger, and is the only significant error for the first few hundred t/M. The error estimate from the loss of mass during the simulation is negligible, even at its maximum value, which occurs after t_{peak} (the time of the merger), indicated in the plots by the vertical dashed line.

In Fig. 5, we compare the phase difference between different resolutions for the hMlR $q = 1.2$ systems using the ShTS time stepping. In Fig. 6, we do the same for the lMhR $q = 1.0$ case using the SpTS algorithm. As mentioned in the methods section, we note that time stepping errors are not significant in these simulations; the SpTS simulations however take advantage of their reduced cost to use different definitions of low, mid, and high spatial resolutions, which leads to different behaviors of the phase error. Specifically, the LR SpTS is about halfway between the LR and MR ShTS resolutions on the finite difference grid (but the same accuracy requirements on the pseudo-spectral grid). These figures illustrate the two potential impact of partial error cancellations in SpEC and the need to use the fairly conservative error estimates described above. Figure 5 shows what appears to be far better than third-order convergence of the solution, while Fig. 6 appears to show poor convergence of the solution. This is because in the first case, error cancellation affects the comparison between the MR and HR simulations (as can be seen from the times at which the phase difference between these simulations goes to zero), while in the second, it likely affects (more subtly) the difference between the LR and MR simulations (although the lack of zero crossing
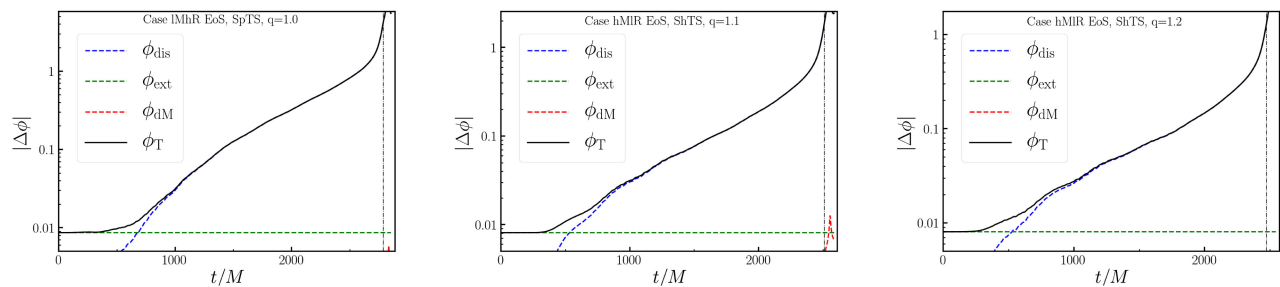

FIG. 4. Phase error estimates for the (2, 2) mode of the $q = 1.0$ SpTS, $q = 1.1$ ShTS, and $q = 1.2$ ShTS binaries, broken down by sources: finite resolution (ϕ_{dis}), extrapolation error (ϕ_{ex}), and error from mass loss (ϕ_{dM}), with the vertical dashed line indicating the peak of the gravitational wave amplitude (merger).
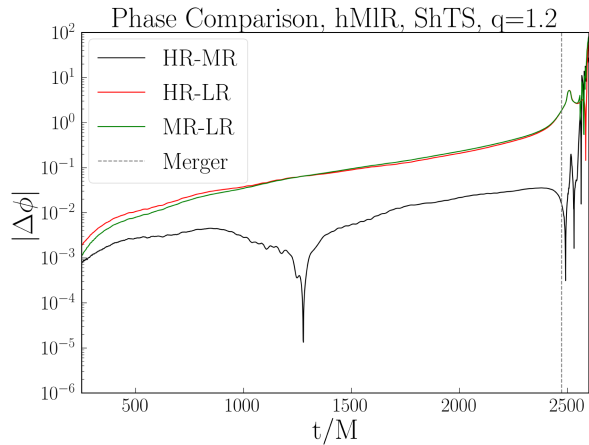
FIG. 5. Comparison of phases for the extrapolated gravitational waves at three resolutions for the $q = 1.2$ hMlR ShTS waveforms. There is minimal difference between the MR and HR phases during the simulation. This is clearly due to cancellation of errors, with a $\Delta\phi = 0$ crossing at $t \sim 1300M$ (a similar behavior is seen in the $q = 1.1$ case). There is exact error cancellation at $t \sim 1300M$ and thus presumably partial error cancellations at other times.
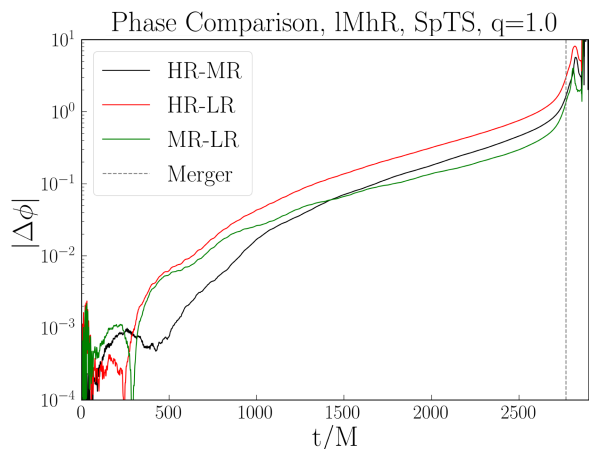

FIG. 6. Difference of phases for the extrapolated gravitational waves of the lMhR SpTS $q = 1.0$ waveforms. Given the error cancellation observed in Fig. 5, the change in slope of the phase difference between the LR and MR simulations likely indicate partial cancellation of errors between these simulations at late times—although the lack of zero-crossing makes it impossible to fully confirm this interpretation here.

makes it impossible to fully verify this interpretation of the errors in this case). The overall outcome for our error estimates remains the same however: We base our estimates on the pair of simulations predicting the largest error (which we interpret as the simulations with the least error cancellation) and assuming an order of convergence slower than that of any part of our algorithm. We then check that this method provides reasonable results by verifying that error estimates for simulations of different lengths (the

SpTS and ShTS simulations), different mass ratios, and different spectral equations of state are consistent.

B. Discussion

Given the relatively minimal database of similar BNS simulations, we compare the accuracy of our simulations to the BNS simulations in Foucart *et al.* (2019) [36]. We note that this comparison is provided mostly for context, as we have to consider simulations with different initial separations—an apples-to-apples comparison of the accuracy of the spectral equation of state with piecewise polytropic equations of state and single polytropes was however performed in [9] over shorter timescales and offered similar conclusions. The simplest points of comparisons are the equal mass systems from this manuscript and the two equal mass BNS systems from [36]: a 12.5 orbit long simulation using a $\Gamma = 2$ polytrope and an 8.5 orbit long simulation using the piecewise polytropic MS1b equation of state. All simulations have the same mass ratio and, in addition, the $\Gamma = 2$ case of [36] and the lMhR simulation from this work have similar tidal deformabilities (10% difference). The $\Gamma = 2$ simulation has a resolution nearly identical to that used in this manuscript, while the MS1b equation of state uses a 20% coarser resolution. We can see that our total error at the merger here is comparable to the $q = 1.0$ simulations performed with the piecewise polytropic EOS MS1b and slightly higher than for the single polytrope with $\Gamma = 2$ case. However, the MS1b evolved for 8.5 orbits, significantly shorter than our present simulations of about 10.5 for the ShTS and 11.5 for the SpTS, which themselves are shorter than the 12.5 orbits of the single polytrope simulation. This is consistent with expectations that the spectral EOS accumulates errors slower than the MS1b EOS and faster than the polytropic EOS.

More interestingly, we can use our simulations to test the agreement between numerical results and semianalytical waveforms. Here, we compare our two ShTS systems against two analytical models, IMRPhenomD_NRTidalv2 and SEOBNRv4Tidal, generated using the LALSuite [37]. Both analytical models were generated using our simulations' parameters (ADM mass, tidal deformability, etc.) and show a high level of agreement in waveforms during inspiral, and some deviations beyond estimated numerical errors at the time of the merger (see Figs. 7 and 8, discussed below). In order to perform meaningful comparisons with analytical models and between simulations of different lengths or using different equations of state, the gravitational waves from our simulations are time and phase matched to the HR resolution simulations by choosing two set times in the reference waveform and minimizing the phase difference within that time frame among all transformations $t' = t + \delta t$, $\phi' = \phi + \delta\phi$. We do this after interpolating all waveforms to a common set of retarded times using a cubic 1D interpolator.
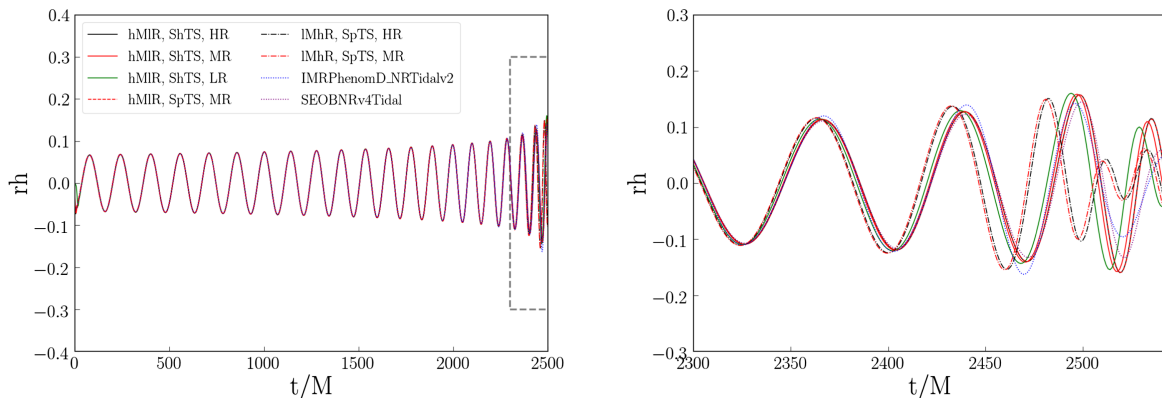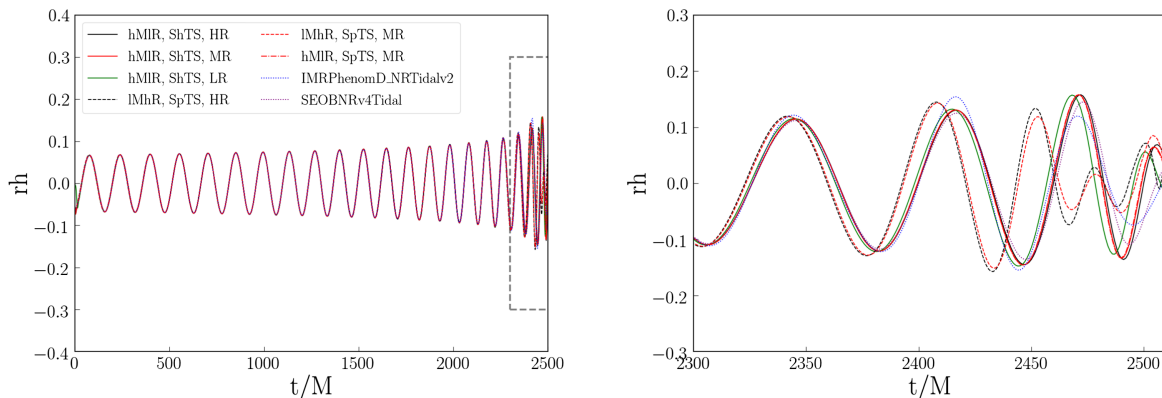
FIG. 7.   Gravitational wave signals for the $q = 1.1$ simulations. We show three resolutions for the hMlR ShTS $q = 1.1$ simulations, one from the hMlR SpTS $q = 1.1$, two from the lMhR SpTS $q = 1.1$ simulations, and two from the analytical models IMRPhenomD_NRTidalv2 and SEOBNRv4 generated for the hMlR EOS. The dashed gray square indicates the zoomed in plot to the right. It can be seen at the merger a clear distinction between the lMhR EOS and the hMlR EOS. Even the LR system with a relatively large error is still visibly distinct from the lMhR systems. This demonstrates that we are able to distinguish between two closely related EOSs (numerically, this does not mean that such a difference is observable by current GW detectors). We can also see close matching to the analytical models until just before the merger, when slightly larger differences arise.

FIG. 8.   Gravitational wave signals for the $q = 1.2$ simulations. We show three resolutions from the hMlR ShTS, one from the hMlR SpTS simulation, two from lMhR SpTS, and finally two from the analytical models IMRPhenomD_NRTidalv2 and SEOBNRv4 generated for the hMlR EOS. We see a clear difference between the hMlR EOS and the lMhR EOS, as in the $q = 1.1$ case above. The analytical models also closely match our simulations, until the merger.

We can see in Figs. 7 and 8 the analytical and numerical relativity waveforms overlaid, and, for waveforms using the same equation of state, the close agreement between them during the inspiral and plunge phases of the simulation. Differences between simulations and models are most apparent near the merger, but this is not unexpected as analytical models often do not accurately predict the merger portion of simulations. Simulations using different equations of state are clearly distinguishable at the merger on these plots. Using the peak amplitude of the extrapolated and analytical waveforms as the merger time, we can see in Fig. 9 that the SEOBNRv4Tidal analytical model has an oscillatory amplitude before the merger and reaches the merger before the other hMlR $q = 1.1$ systems. We see similar behavior for the $q = 1.2$ systems.

As an additional avenue of waveform analysis, we use a new method from Read (2023) [38]. Gravitational waves are Fourier transformed using the stationary phase approximation and matched in time and phase at a reference coalescence frequency f_c (chosen to be the minimum peak frequency among our simulations and analytical models in our analysis). We then compare the resulting phase differences of the Fourier transform. This matching procedure can be better understood if we note that applying a time and phase shift on these waveforms allows us to change the Fourier phase according to $\phi(f) \to \phi(f) + Af + B$ for any constant A, B; i.e., from a practical point of view, the spectral phases of two waveforms $\phi(f)$ are only distinguishable if they differ in their curvature $d^2\phi/df^2$; any difference of the type $\delta\phi = Af + B$ can be removed by
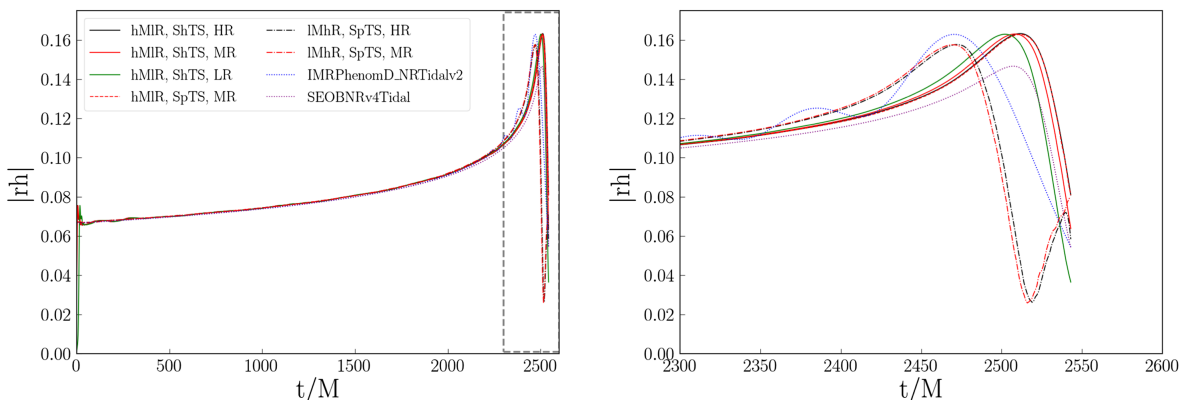
FIG. 9. Amplitude of the gravitational waves of the hMlR ShTS $q = 1.1$ systems, the hMlR SpTS $q = 1.1$ system, two lMhR SpTS $q = 1.1$ simulations, and the $q = 1.1$ hMlR SEOBNRv4Tidal and IMRPhenomD_NRTidalv2 models, after allowing for a time and phase shift minimizing differences at early times. The dashed gray square indicates the area covered by the plot to the right, which focuses on the merger.

applying an appropriate phase and/or time shift. When matching the time and phase of two waveforms at a specific frequency f_c, we effectively match the values of $\phi(f_c)$, $d\phi/df(f_c)$ for these waveforms.

Quite importantly, the method is constructed so that the phase difference is fairly insensitive to numerical noise in the calculation of frequencies and of their derivatives and relies on the choice of a single reference frequency for matching waveforms. In [38], a variation of this method is also used to assess whether waveforms are distinguishable in various gravitational wave detectors—however, this requires knowledge of the waveforms over the entire frequency range accessible to the detector, while our numerical waveforms only provide data for $f \gtrsim 400$ Hz. Another important advantage of this method is that it is relatively insensitive to errors in the early phase of the evolution, when simulations can have a hard time resolving high-frequency noise and instead provide a more direct comparison of waveforms in the range in which finite size effects are the largest.

The results of this analysis are shown on Fig. 10. Here, we show spectral phase differences with respect to the analytical SEOBNRv4Tidal model of the lMhR system after matching at $f_c = 1514$ Hz, the lowest peak frequency among all the plotted waveforms. We emphasize again that waveforms are only distinct on this plot if they differ in their second derivative $\frac{d^2\phi}{df^2}$—any difference linear in f could be removed with an appropriate time and phase shift. In this case, the waveforms only clearly differ at high frequency ($f \gtrsim 900$ Hz).

Looking at this figure in more detail, the bottom solid green line shows the high resolution hMlR ShTS simulation, with the surrounding gray and green filled-in area indicating two levels of estimated error, obtained by assuming second-order convergence between the HR and LR simulations ($\pm\Delta\phi_{2-0}$) or the HR and MR simulations ($\Delta\phi_{2-1}$). The top "dash-dot" green line is the HR lMhR

simulation, with its own error estimate $\pm\Delta\phi_{2-1}$. We see that after matching the waveforms at late times, the results show cleaner convergence than for the "raw" numerical error. More specifically, in this figure, the fact that both error estimates agree when assuming second-order convergence (especially for $f \gtrsim (500$–$600)$ Hz) means that all three simulations are indeed consistent with second-order convergence of the results in that frequency range. The hMlR SEOBNRv4Tidal model, lying within the filled in area around the hMlR HR line, is consistent with the hMlR numerical simulations. This is not the case for the lMhR simulation, for which the SEOBNRv4Tidal model lies well
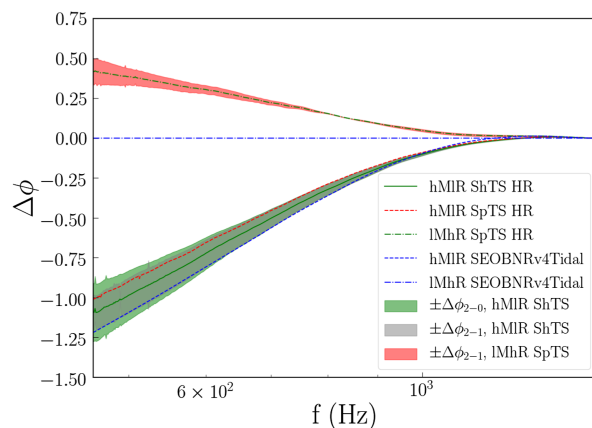

FIG. 10. Phase error between the lMhR SEOBNRv4Tidal analytical model and other simulations/models as a function of frequency. In this plot, we use the methods of analysis from [38], Eq. 19(b) in particular. The filled-in areas are defined by $\Delta\phi_{2-1} = 1.77|\phi_{HR} - \phi_{MR}|$ and $\Delta\phi_{2-0} = 0.7|\phi_{HR} - \phi_{LR}|$, i.e., errors assuming second-order convergence of the simulations. In this analysis, we choose as reference frequency $f_c = 1514$ Hz, the lowest value of maximum frequency among our simulations and analytical models (the analysis effectively assumes that all simulations are at the same time and phase when reaching that frequency).

outside of estimated numerical errors (i.e., the filled in red area around the lMhR HR line). We note however that this should not be interpreted as a better agreement between SEOBNRv4Tidal and numerical relativity for the hMlR equation of state. Rather, this is due to the fact that, in this plot, we are matching waveforms at the peak frequency of the lMhR configuration, which is about 100 Hz below the peak frequency of the hMlR configuration. As a result, we excluded from our analysis the portion of the hMlR waveform where differences between SEOBNRv4Tidal and numerical relativity are the largest. A similar comparison matching waveforms at the peak frequency of the hMlR configuration shows the SEOBNRv4Tidal model to be inconsistent with the numerical simulations at late times for the hMlR equation of state as well. This is another clear indication that any difference between the SEOBNRv4Tidal model and the numerical result is due to the behavior of the SEOBNRv4Tidal model close to the merger. Additionally we see that our simulations can clearly distinguish between the hMlR and lMhR EOSs. However, we must note that the difference between the two EOSs mostly comes from the behavior of the waveform above ~800 Hz, outside the most sensitive range of LIGO and Virgo. Accordingly, these results do not indicate anything about the detectability of these differences by current gravitational wave detectors. They only tell us that the numerical relativity waveforms are distinguishable well outside of their numerical errors.

Similarly, in Figs. 7 and 8, we are clearly able to see a distinct phase difference between our hMlR EOS and the lMhR EOS within our estimated numerical error. Assuming a linear dependence of the phase at the merger in $\tilde{\Lambda}$, and for the specific EOS and mass ratios simulated in this manuscript, we estimate that we are able to distinguish with SpEC the phase of the gravitational waveforms at the merger for different spectral equations of state down to a dimensionless tidal deformability difference of $\Delta\tilde{\Lambda} \approx 55$, well below current constraints from the observation of GW170817 [32]. This shows that the spectral EOS is a promising option to train analytical models. This is of course a rough approximation, as we have only considered a narrow range of tidal deformabilities. Anecdotally, we have seen higher accuracy in SpEC simulations for which tidal effects were small (e.g., in the older BHNS simulations of [39], where tides are entirely negligible), but this is likely a small effect over the narrower range of effective tidal deformabilities probed by near equal mass BNS systems.

In Figs. 7 and 8, we also compare results with both time stepping methods. We see a very close agreement in the extrapolated waveforms using the ShTS method and the SpTS method for simulations with otherwise identical mass ratios and equations of state. In both the $q = 1.1$ and $q = 1.2$ cases, the SpTS and ShTS simulations behave nearly identically in waveform and peak amplitude at the

merger, with differences well below our estimated numerical errors. This is reassuring considering that these simulations were performed from different initial separations, with different time stepping methods, and with different grid resolutions.

The ShTS and SpTS simulations were run on different clusters, specifically the University of Texas' Frontera cluster and the University of New Hampshire's Plasma cluster. From standardized speed tests performed on both machines for BNS evolutions, we have determined that Frontera is roughly 12% faster than Plasma, but a direct comparison of computational cost is nontrivial.

We therefore compare two main components to estimate computational cost: the number of time steps the grid evolving Einstein's equations took and the CPU hours spent during the $\Delta t = 5000$ (about 0.025 seconds) preceding the merger. Using this time period will avoid the initial numerical errors and junk radiation at simulation start from affecting the computational time, as well as the extra orbit in the SpTS case. We compared the MR $q = 1.1$ simulations.

We found the ShTS simulation to have taken 251823 steps during this $\Delta t = 5000$ period and cost 60341 CPU hours. In comparison, the SpTS took 357506 steps, with only a cost of 42707 CPU hours. We also must note that the SpTS simulation had an approximately 10% increase in resolution compared to the ShTS case, which should result, everything else being equal, in approximately 40% increased computational expense for the fluid evolution. Despite this additional cost and approximately 42% additional time steps for the evolution of Einstein's equations, we can see an approximately 30% reduction in computational time cost in the SpTS case. Taking into account that the ShTS simulations were run on the faster Frontera cluster, and the SpTS simulations on the slower Plasma cluster, this is a strong indication that the SpTS method does indeed have a significant beneficial impact on simulation costs. While this comparison is relatively rough, we find it sufficient to state that the SpTS method does save on computational resources in simulations such as the ones used in this paper.

IV. CONCLUSION

From our work, we have found the spectral EOS to be a promising option for numerical BHNS or BNS waveform studies. It is capable in our systems to generate gravitational waves from BNS that agree within expected error with state-of-the-art analytical models up to the merger event, where analytical models become less accurate. The defining parameters of spectral EOSs can be adjusted to produce a range of neutron star EOS candidates, offering a large amount of flexibility for future systems as we further refine the constraints on the EOS of a neutron star. It offers an improved ability to generate stars with appropriate macroscopic properties when

compared with a polytropic EOS and provides better numerical accuracy compared to a discontinuous EOS, at least in the SpEC code.

We find in particular that, for two distinct methods of matching the waveforms in time and phase, we are capable of clearly capturing differences in the gravitational wave signals produced by binaries with tidal deformabilities of $\tilde{\Lambda} \approx 550$ and $\tilde{\Lambda} = 700$. Assuming a linear dependence of the phase differences with $\tilde{\Lambda}$, our results indicate that variations of $\Delta\tilde{\Lambda} \approx 55$ could lead to numerical waveforms whose behavior close to the merger differ by more than our current finite-resolution errors.

As for numerical methods, our preliminary comparison between the SpTS and ShTS methods indicates potential computational cost savings by uncoupling the finite difference and spectral grid time steps. In this manuscript, we measured a greater than 30% decrease in CPU hours used for a simulation with $\approx 10\%$ increased resolution on a cluster with slower hardware. Clearly, further testing on simulations conducted on the same cluster, utilizing the same simulation parameters such as resolution and initial conditions, is required for a definitive answer, but our test here has shown the comparison to be worth closer inspection of a method that could potentially have significant savings in computational cost. We note that this is largely possible because the time step in our simulations is limited by stability considerations, and discretization in time is generally a subdominant source of error.

There is still a great deal of experimentation that can be done with the spectral EOS, including higher resolution simulations to verify the accuracy of our current error estimates. Additionally, generating NS with varying radii, mass, and tidal deformability by adjusting the Γ_0, η_2, η_3, Γ_{th}, ρ_0, and P_0 may prove useful in determining its viability in a range of systems, allowing for a smooth EOS for SpEC and other codes sensitive to discontinuous EOSs. The spectral EOS offers a new avenue for simulations, expanding our potential tools for more accurate and better resolved simulations, to aid in eventually better understanding the detected gravitational waves from merger events between compact objects.

[1] B. P. Abbott (The LIGO Scientific and The Virgo Collaborations), GW150914: The advanced LIGO detectors in the era of first discoveries, arXiv:1602.03838 [Phys. Rev. Lett. (to be published)].

[2] B. P. Abbott (The LIGO Scientific and The Virgo Collaborations), Search for postmerger gravitational waves from the remnant of the binary neutron star merger GW170817, Astrophys. J. **851**, L16 (2017).

[3] B. P. Abbott (The LIGO Scientific and The Virgo Collaborations), GW190425: Observation of a compact binary coalescence with total mass $\sim 3.4 M_{\odot}$, Astrophys. J. Lett. **892**, L3 (2020).

[4] R. Abbott (The LIGO Scientific and The Virgo Collaborations), Observation of gravitational waves from two neutron star–black hole coalescences, Astrophys. J. Lett. **915**, L5 (2021).

[5] R. Abbott *et al.* (The LIGO Scientific, The Virgo, and The KAGRA Collaborations), Gwtc-3: Compact binary coalescences observed by ligo and virgo during the second part of the third observing run, Phys. Rev. X **13**, 041039 (2023).

[6] R. Abbott (The LIGO Scientific and The Virgo Collaborations), GW190814: Gravitational waves from the coalescence of a 23 solar mass black hole with a 2.6 solar mass compact object, Astrophys. J. Lett. **896**, L44 (2020).

[7] D. Radice, L. Rezzolla, and F. Galeazzi, High-order fully general-relativistic hydrodynamics: New approaches and tests, Classical Quantum Gravity **31**, 075012 (2014).

[8] G. Doulis, F. Atteneder, S. Bernuzzi, and B. Brügmann, Entropy-limited higher-order central scheme for neutron star merger simulations, Phys. Rev. D **106**, 024001 (2022).

[9] F. Foucart, M. Duez, A. Gudinas, F. Hébert, L. Kidder, H. Pfeiffer, and M. Scheel, Smooth equations of state for

high-accuracy simulations of neutron star binaries, Phys. Rev. D **100,** 104048 (2019).

[10] C. A. Raithel and V. Paschalidis, Improving the convergence order of binary neutron star merger simulations in the baumgarte- shapiro-shibata-nakamura formulation, Phys. Rev. D **106,** 023015 (2022).

[11] B. P. Abbott (The LIGO Scientific and The Virgo Collaborations), GW170817: Measurements of neutron star radii and equation of state, Phys. Rev. Lett. **121,** 161101 (2018).

[12] G. Raaijmakers, S. K. Greif, T. E. Riley, T. Hinderer, K. Hebeler, A. Schwenk, A. L. Watts, S. Nissanke, S. Guillot, J. M. Lattimer, and R. M. Ludlam, Constraining the dense matter equation of state with joint analysis of NICER and LIGO/virgo measurements, Astrophys. J. **893,** L21 (2020).

[13] G. Raaijmakers, S. K. Greif, K. Hebeler, T. Hinderer, S. Nissanke, A. Schwenk, T. E. Riley, A. L. Watts, J. M. Lattimer, and W. C. G. Ho, Constraints on the dense matter equation of state and neutron star properties from NICER's mass–radius estimate of PSR J0740 + 6620 and multimessenger observations, Astrophys. J. Lett. **918,** L29 (2021).

[14] Z. Carson, A. W. Steiner, and K. Yagi, Constraining nuclear matter parameters with GW170817, Phys. Rev. D **99,** 043010, (2019).

[15] Z. Carson, A. W. Steiner, and K. Yagi, Future prospects for constraining nuclear matter parameters with gravitational waves, Phys. Rev. D **100,** 023012 (2019).

[16] M. F. O'Boyle, C. Markakis, N. Stergioulas, and J. S. Read, A parametrized equation of state for neutron star matter with continuous sound speed, Phys. Rev. D **102,** 083027 (2020).

[17] I. Legred, Y. Kim, N. Deppe, K. Chatziioannou, F. Foucart, F. Hébert, and L. E. Kidder, Simulating neutron stars with a flexible enthalpy-based equation of state parametrization in SpECTRE, Phys. Rev. D **107,** 123017 (2023).

[18] C. A. Raithel, P. Espino, and V. Paschalidis, Finite-temperature effects in dynamical spacetime binary neutron star merger simulations: Validation of the parametric approach, Mon. Not. R. Astron. Soc. **516,** 4792 (2022).

[19] C. A. Raithel, F. Özel, and D. Psaltis, Finite-temperature extension for cold neutron star equations of state, Astrophys. J. **875,** 12 (2019).

[20] Spectral einstein code, https://www.black-holes.org/code/SpEC.html.

[21] L. Lindblom, M. A. Scheel, L. E. Kidder, R. Owen, and O. Rinne, A new generalized harmonic evolution system, Classical Quantum Gravity, **23,** S447 (2006).

[22] B. Szilágyi, Key elements of robustness in binary black hole evolutions using spectral methods, Int. J. Mod. Phys. D, **23,** 1430014 (2014).

[23] D. Radice and L. Rezzolla, THC: A new high-order finite-difference high-resolution shock-capturing code for special-relativistic hydrodynamics, Astron. Astrophys. **547,** A26 (2012).

[24] F. Foucart, M. B. Deaton, M. D. Duez, L. E. Kidder, I. MacDonald, C. D. Ott, H. P. Pfeiffer, M. A. Scheel, B. Szilagyi, and S. A. Teukolsky, Black-hole–neutron-star mergers at realistic mass ratios: Equation of state and spin orientation effects, Phys. Rev. D **87,** 084006 (2013).

[25] M. D. Duez, F. Foucart, L. E. Kidder, H. P. Pfeiffer, M. A. Scheel, and S. A. Teukolsky, Evolving black hole-neutron star binaries in general relativity using pseudospectral and finite difference methods, Phys. Rev. D **78,** 104015 (2008).

[26] S. C. Noble, C. F. Gammie, J. C. McKinney, and L. Del Zanna, Primitive variable solvers for conservative general relativistic magnetohydrodynamics, Astrophys. J. **641,** 626 (2006).

[27] L. Lindblom, Spectral representations of neutron-star equations of state, Phys. Rev. D **82,** 103011, (2010).

[28] H. P. Pfeiffer, L. E. Kidder, M. A. Scheel, and S. A. Teukolsky, A multidomain spectral method for solving elliptic equations, Comput. Phys. Commun. **152,** 253 (2003).

[29] F. Foucart, L. E. Kidder, H. P. Pfeiffer, and S. A. Teukolsky, Initial data for black hole–neutron star binaries: A flexible, high-accuracy spectral method, Phys. Rev. D **77,** 124051 (2008).

[30] R. Haas, C. D. Ott, B. Szilagyi, J. D. Kaplan, J. Lippuner, M. A. Scheel, K. Barkett, C. D. Muhlberger, T. Dietrich, M. D. Duez, F. Foucart, H. P. Pfeiffer, L. E. Kidder, and S. A. Teukolsky, Simulations of inspiraling and merging double neutron stars using the spectral einstein code, Phys. Rev. D **93,** 124062 (2016).

[31] H. P. Pfeiffer, D. A. Brown, L. E. Kidder, L. Lindblom, G. Lovelace, and M. A. Scheel, Reducing orbital eccentricity in binary black hole simulations, Classical Quantum Gravity **24,** S59 (2007).

[32] B. P. Abbott (The LIGO Scientific and The Virgo Collaborations), GW170817: Observation of gravitational waves from a binary neutron star inspiral, Phys. Rev. Lett. **119,** 161101 (2017).

[33] M. Boyle and A. H. Mroué, Extrapolating gravitational-wave data from numerical simulations, Phys. Rev. D **80,** 124045 (2009).

[34] F. Foucart, A. Chernoglazov, M. Boyle, T. Hinderer, M. Miller, J. Moxon, M. A. Scheel, N. Deppe, M. D. Duez, F. Hébert, L. E. Kidder, W. Throwe, and H. P. Pfeiffer, High-accuracy waveforms for black hole-neutron star systems with spinning black holes, Phys. Rev. D **103,** 064007 (2021).

[35] M. Boyle, D. A. Brown, L. E. Kidder, A. H. Mroué, H. P. Pfeiffer, M. A. Scheel, G. B. Cook, and S. A. Teukolsky, High-accuracy comparison of numerical relativity simulations with post-newtonian expansions, Phys. Rev. D **76,** 124038 (2007).

[36] F. Foucart, M. Duez, T. Hinderer, J. Caro, A. R. Williamson, M. Boyle, A. Buonanno, R. Haas, D. Hemberger, L. Kidder, H. Pfeiffer, and M. Scheel, Gravitational waveforms from spectral einstein code simulations: Neutron star-neutron star and low-mass black hole-neutron star binaries, Phys. Rev. D **99,** 044008, (2019).

[37] LIGO Scientific Collaboration, LIGO Algorithm Library—LALSuite free software (GPL), 2018.

[38] J. S. Read, Waveform uncertainty quantification and interpretation for gravitational-wave astronomy, Classical Quantum Gravity **40,** 135002 (2023).

[39] F. Foucart, L. Buchman, M. D. Duez, M. Grudich, L. E. Kidder, I. MacDonald, A. Mroue, H. P. Pfeiffer, M. A.

Scheel, and B. Szilagyi, First direct comparison of non-disrupting neutron star-black hole and binary black hole merger simulations, Phys. Rev. D **88**, 064017 (2013).

[40] D. Stanzione, J. West, R. T. Evans, T. Minyard, O. Ghattas, and D. K. Panda, Frontera: The evolution of leadership computing at the national science foundation, in *Practice and Experience in Advanced Research Computing, PEARC '20, New York, NY* (Association for Computing Machinery, New York, NY, 2020), pp. 106–111.